Simulation of electron beam instabilities in collisionless plasmas

C. Y. ZHENG, Z. J. LIU, A. Q. ZHANG, S. P. ZHU and X. T. HE

Institute of Applied Physics and Computational Mathematics, PO Box 8009,
Beijing 100088, People's Republic of China
(zheng_chunyang@iapcm.ac.cn)

Abstract. The influence of self-generated magnetic and electric fields on the transport of relativistic electrons in dense plasmas was studied using a particle-in-cell simulation. For conditions relevant to the fast ignitor, the laser-driven relativistic electrons may have significant energy spread along or perpendicular to the propagation direction of the beams. The effect of electron energy spread on the growth rate, the occurrence threshold of both the Weibel-like filamentation instability and the electrostatic two-stream instability and the competition between them were investigated. The Weibel instability results in the formation of a magnetic channel, which may collimate inward fast electrons without significant deviation, and the excitation of a longitudinal electric field due to two-stream instability is destructive to the stability of the magnetic channel. The generation of relativistic electrons by the interaction of a high-intensity laser beam at the vacuum–dense plasma boundary and propagation of the electrons in the dense plasma were studied using a three-dimensional particle-in-cell code. It is shown that the electron velocity spread owing to transverse collective heating saturates the magnetic field and the longitudinal electrostatic field may play a dominant role in limiting the stable propagation of fast electrons into over-dense plasmas.

1. Introduction

Fast ignition (FI), as a novel ignition concept for inertial confinement fusion, has been studied extensively in recent years [1,2]. Two of the critical issues for FI are the decay of the intense laser beam and the collimation of the relativistic electron beam (REB) in a relatively long plasma channel. In the interaction of a high-intensity laser with the plasma, the forward fast electron current generated near the critical plasma density always exceeds the Alfvén current limit and must be neutralized by a cold return current to allow the REB to propagate unimpeded into the dense plasma [3]. Two types of instabilities will grow in such a counter-streaming system due to the anisotropic electron velocity distribution. One is the electromagnetic Weibel-like filamentation instability (WFI) [4] and the other is the electrostatic two-stream instability (ETSI). Microscopic instabilities in a beam plasma occur mainly in mildly dense plasma near the laser–plasma interface ($<10^{22}$ cm^{-3}), but they may prevent the conditions for burn from being met in the compressed core of the pellet by broadening the region where fast electrons deposit their energy [5, 6]. In this paper, we illustrate the main features of WFI and ETSI of electron

beams propagating in dense plasmas. In reality, the energy distribution of beam electrons is complicated with significant energy spread along or perpendicular to the propagation direction of the beams owing to different generation or acceleration mechanisms [7]. The effect of the energy spread of beam electrons on the onset and nonlinear coupling of WFI and ETSI was investigated using fully relativistic electromagnetic particle-in-cell (PIC) codes. The energy spread of beam electrons along the propagation direction of the beams mainly influences the growth rate of ETSI and the growth of WFI can be significantly suppressed if the transverse energy spread of the electrons is large enough. The dominant factors limiting the stable and deep propagation of relativistic electrons in dense plasmas are discussed.

This paper is organized as follows. In Sec. 2, analytical results relevant to the effect of beam energy spread on the linear growth rate and the occurrence threshold of WFI and ETSI are given. In Sec. 3, the effect of beam energy spread on the competing and nonlinear coupling of WFI and ETSI are first given using a two-dimensional (2D) PIC code, and then the generation of REB by the interaction of a high-intensity laser beam at the dense plasma boundary and propagation of the electrons in the dense plasma are studied using a three-dimensional (3D) PIC code. Our conclusions are given in Sec. 4.

2. Theoretical results

The configuration of two electron streams, though the total net current is zero, is unstable and could feed electrostatic modes (perturbation wave vector $\mathbf{k}$ parallel to the beam) with the excitation of the electrostatic field and electromagnetic modes ($\mathbf{k}$ normal to the beam) accompanying the generation of a magnetic field in the direction perpendicular to $\mathbf{k}$ and the beam velocity. The competing and nonlinear coupling of these two types of instabilities (WFI and ETSI) are intrinsically a feature of multi-dimensional systems, especially when the characteristic transverse and longitudinal scales are comparable. In this section, the linear growth rate and the instability threshold of WFI and ETSI relevant to the presence of beam energy spread are presented.

The dispersion relation of ETSI can be obtained for a counter-streaming electron distribution $f_0(\mathbf{p})$ [8],

$$f_0(\mathbf{p}) = \frac{1}{4\pi v_{\text{eth}}^2}[n_1\delta(p_x - p_{x10}) + n_2\delta(p_x - p_{x20})]\exp\left(-v_\perp^2/2v_{\text{eth}}^2\right) \tag{1}$$

$$\frac{n_1}{\gamma_1^3(\omega - k_x v_{x10})^2} + \frac{n_2}{\gamma_2^3(\omega - k_x v_{x20})^2} = 1 \tag{2}$$

where n_1 and n_2 are the densities of the beams, v_{x10} and v_{x20} are the mean velocities in the beam flow direction and v_{eth} is the thermal velocity of the beam electrons in the transverse direction. Assuming $n_1 + n_2 = n_0(\omega_{\text{pe0}}^2)$, $\omega_{\text{pe0}} = (4\pi e^2 n_0/m_e)^{1/2}$ and $n_1 v_{x10} + n_2 v_{x20} = 0$. Temporal and spatial scales are normalized to the inverse electron plasma frequency ω_{pe0}^{-1} and the collisionless skin depth c/ω_{pe0}. The relation between the linear growth rate and the wave vector of the perturbation can be obtained from (2). Figure 1 shows the relation between the linear growth rate ω_{Im} and the perturbation wave number k in two cases: (1) $v_{x10} = 0.8c, v_{x20} = -0.24c$ and (2) $v_{x10} = 0.95c, v_{x20} = -0.285c$, with $\alpha = n_1/n_2 = 0.3$. ETSI is stabilized at short wavelengths, i.e. there exists a threshold wave number k_c. It can be seen that both the maximum growth rate and the maximum unstable wave number decrease
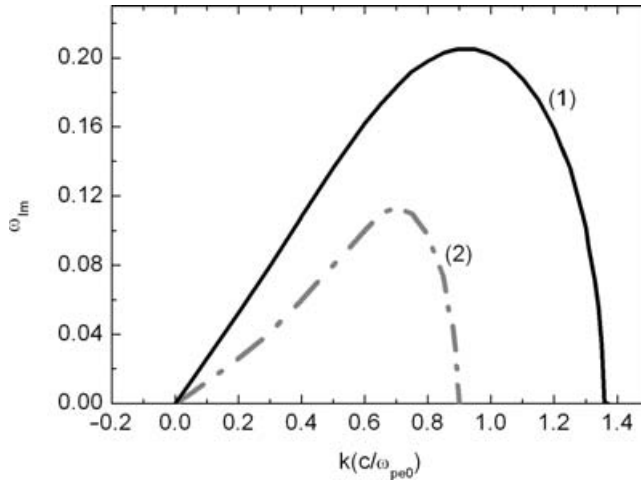
Figure 1. Normalized linear growth rate of TSI as a perturbation wave number for $\alpha = 0.3$ in two cases: curve 1, $v_{x10} = 0.8c$, $v_{x20} = -0.24c$ and curve 2, $v_{x10} = 0.95c$, $v_{x20} = -0.285c$.

when the relativistic effect becomes important. However different to the above cold-beam limit, the spread of thermal velocity about v_{x10} results in the reduction of the ETSI growth rate and even suppresses the occurrence of ETSI [9]. Detailed discussion concerning the kinetic effect on ETSI is given in the next section using a numerical simulation.

The physics of WFI in the linear stage was obtained by employing the relativistic kinetic theory model developed in [10]. Let us assume the electrons obey a normalized zero-order distribution function

$$f_0 = n_1 F_1 + n_2 F_2 \tag{3}$$

with

$$F_{1(2)} = \frac{1}{2P_{z0}} \delta\big(P_x - P_{x01(2)}\big)\delta(P_y)[\Theta(P_z + P_{z0}) - \Theta(P_z - P_{z0})] \tag{4}$$

where $\Theta(x)$ is a step function, and for this distribution function, the dispersion relation for the purely transverse modes (**k** parallel to $\hat{z}$) obeys [10]

$$\omega^2 - k^2 - n_1 \left\langle \frac{1}{\gamma_1} \right\rangle - n_2 \left\langle \frac{1}{\gamma_2} \right\rangle + \frac{n_1}{\gamma_1} \frac{u_{x01}^2}{1 + u_{x01}^2}$$

$$+ \frac{n_2}{\gamma_2} \frac{u_{x02}^2}{1 + u_{x02}^2} - \frac{n_1 k^2 \beta_{x01}^2 c^2}{\gamma_1\big(\omega^2 - k^2 \beta_{z0}^2 c^2\big)} - \frac{n_2 k^2 \beta_{x02}^2 c^2}{\gamma_2\big(\omega^2 - k^2 \beta_{z0}^2 c^2\big)} = 0 \tag{5}$$

where

$$\left\langle \frac{1}{\gamma_j} \right\rangle = \int dp \frac{F_{j0}}{\gamma} = \frac{1}{2\gamma_1 \beta_{z0}} \ln \frac{1 + \beta_{z0}}{1 - \beta_{z0}}$$

with the standard definitions $u_j = P_j/m_e c$, $\beta_j = P_j/\gamma_j m_e c$, $\gamma_j = (1 + P_{z0}^2/m_e^2 c^2 + P_{x0j}^2/m_e^2 c^2)^{1/2}$.

Using $n_1 \beta_{x01}/\gamma_1 - n_2 \beta_{x02}/\gamma_2 = 0$ and $\beta_{z0} = \beta_{\text{th}0}$, $1 + u_{x0j}^2 = \gamma_{0j}^2 \big(1 - \beta_{z0}^2\big)$, (5) changes as

$$\omega^4 - \big(k^2 c^2 + F + k^2 \beta_{z0}^2\big)\omega^2 + \big(k^2 c^2 + F - G\big)k^2 \beta_{z0}^2 c^2 = 0 \tag{6}$$

where

$$F = \omega_{\text{pe}}^2 \frac{1}{2\beta_{z0}} \ln \frac{1 + \beta_{z0}}{1 - \beta_{z0}} - \omega_{\text{pe}}^2 \frac{\beta_{x01}\beta_{x02}}{1 - \beta_{z0}^2},$$

$$G = \frac{\omega_{\text{pe}}^2 \beta_{x01}\beta_{x02}}{\beta_{z0}^2}, \quad \omega_{\text{pe}}^2 = \frac{4\pi n_1 e^2}{\gamma_1 m} + \frac{4\pi n_2 e^2}{\gamma_2 m}.$$

The threshold conditions for WFI to occur can be established by $G > F$, i.e.

$$\alpha \frac{\gamma_2}{\gamma_1} \beta_{x01}^2 > \frac{\beta_{z0}(1 - \beta_{z0}^2)}{2} \ln \frac{1 + \beta_{z0}}{1 - \beta_{z0}}. \tag{7}$$

In the limit of a cold beam ($\beta_{z0} \ll 1$), a relativistic beam ($u_{x01} \gg 1$), (7) can be simplified to $\alpha > \gamma_1 \beta_{z0}^2 / \beta_{x01}^2$. So for high β_{z0} the WFI can be completely suppressed.

The analytic results relevant to linear growth and the occurrence threshold of ESTI or WFI in a counter-streaming system are presented separately. In the cold-beam limit, WFI always occurs, but there exists a critical threshold for ETSI, i.e. only long enough perturbation wavelengths are unstable. The characteristic transverse and longitudinal system scales and beam conditions will determine which instability is the most unstable one. The competing and nonlinear coupling of these two instabilities will be studied in the next section.

3. Numerical simulations

For conditions relevant to FI, the relativistic electron energy spread along or perpendicular to the propagation direction of the beams is complicated. To study the effect of energy or momentum spread of the beam electrons on the competing and coupling of WFI and ETSI, we first perform 2D PIC simulations, and the numerical procedure used in our PIC code is similar to that given in [11]. The simulations were performed on $x \times y = 128 \times 64$, using a total of 4×10^6 particles. The periodic boundary conditions are imposed in both x and y directions. Temporal and spatial scales in these simulations are normalized to the inverse electron plasma frequency ω_{pe0}^{-1} and the collisionless skin depth c/ω_{pe0}. In these normalized units, the box size is $12.8 \times 6.4(c/\omega_{\text{pe0}})^2$. The ions are protons with mass $m_{\text{i}} = 1836 m_{\text{e}}$. The simulations were initialized with that the two groups of electrons moving in opposite directions with drift velocity $\langle v_{x10} \rangle = 0.8c$, $\langle v_{x20} \rangle = 0.24c$ and $\alpha = n_{\text{e01}}/n_{\text{e02}} = 0.3$.

$$F_{\text{e}0j} = n_{\text{e}0j} C \exp\left[-\left(v_y^2 + v_z^2\right)/2v_{\text{eth}}^2\right] \exp[-(v_x + (-1)^j v_{xj0})^2/2v_\parallel^2], \quad j = 1, 2 \tag{8}$$

where v_{eth} and $v_\parallel$ represent the transverse and longitudinal velocity spread of beam electrons. Initially, the system has no net charge or current and the electric and magnetic fields are set to zero.

Typical images from our 2D simulations are shown in Figs 2–4. Figure 2 shows the temporal evolution of the mean self-generated magnetic field energy and the mean longitudinal electric field energy for three cases ($v_{\text{eth}} = v_\parallel = 0.05c$, $0.15c$ and $v_{\text{eth}} = 0.05c$, $v_\parallel = 0.15c$). Figure 2(a) shows that with the increase of transverse velocity spread for the beam electrons, i.e. v_{eth} changed from $0.05c$ to $0.15c$, the linear growth rate of WFI is reduced from 0.28 to 0.17, and the spread of the longitudinal velocity of the beam electrons does not have an evident effect on the linear growth of the WFI. After the linear stage ($t \geqslant 20\omega_{\text{pe0}}^{-1}$), the magnetic field decays, which is different from lower-dimensional scenarios where only purely Weibel instability is considered [12]. The ETSI can be significant suppressed by the longitudinal electron velocity spread (see Fig. 2(b)). It is shown that for the case where $v_{\text{eth}} = 0.05c$, $v_\parallel = 0.15c$, i.e.
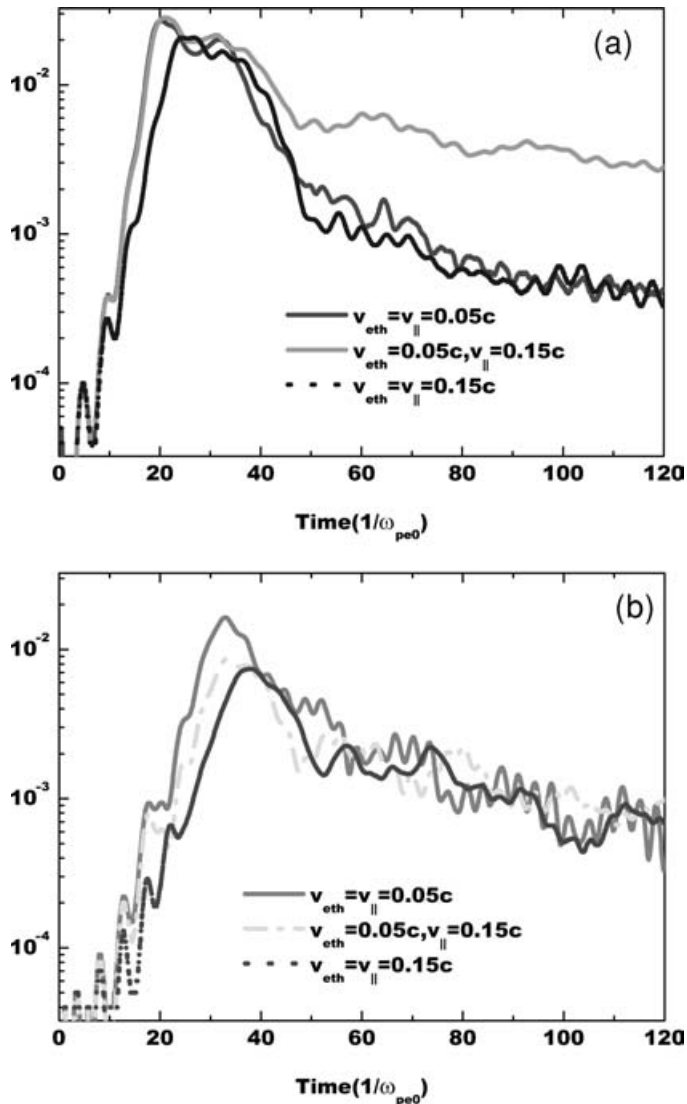
Figure 2. Temporal evolution of (a) the magnetic field energy and (b) the longitudinal electric field energy for different beam electron velocity spreads.

a narrow transverse distribution and a wider longitudinal distribution, the energy of the magnetic field exceeds that of the electric field and the magnetic field drops more slowly after the linear stage. The formation of a larger phase space vortex by electrostatic trapping and the modulation of the magnetic field for two kinds of initial electron distribution are displayed in Figs 3 and 4. Figures 3(a)–(c) show the contours of the magnetic field B_z at three times $t = 20, 30$ and 45 for the parameter $v_{\mathrm{eth}} = v_\parallel = 0.05c$. The magnetic field is in turn negative or positive along the y direction, and the corresponding perturbation wave number is $k_y \cong 1$. From (2), the perturbation wave vector corresponding to the maximum growth rate of ETSI is also $k_x \cong 1$ and the phase velocity of the self-generated electrostatic field E_x is about $0.60c$. The characteristic scales for these two instabilities are comparable. Figures 3(d)–(f) show the electron distribution in the (v_x, x) phase space at three
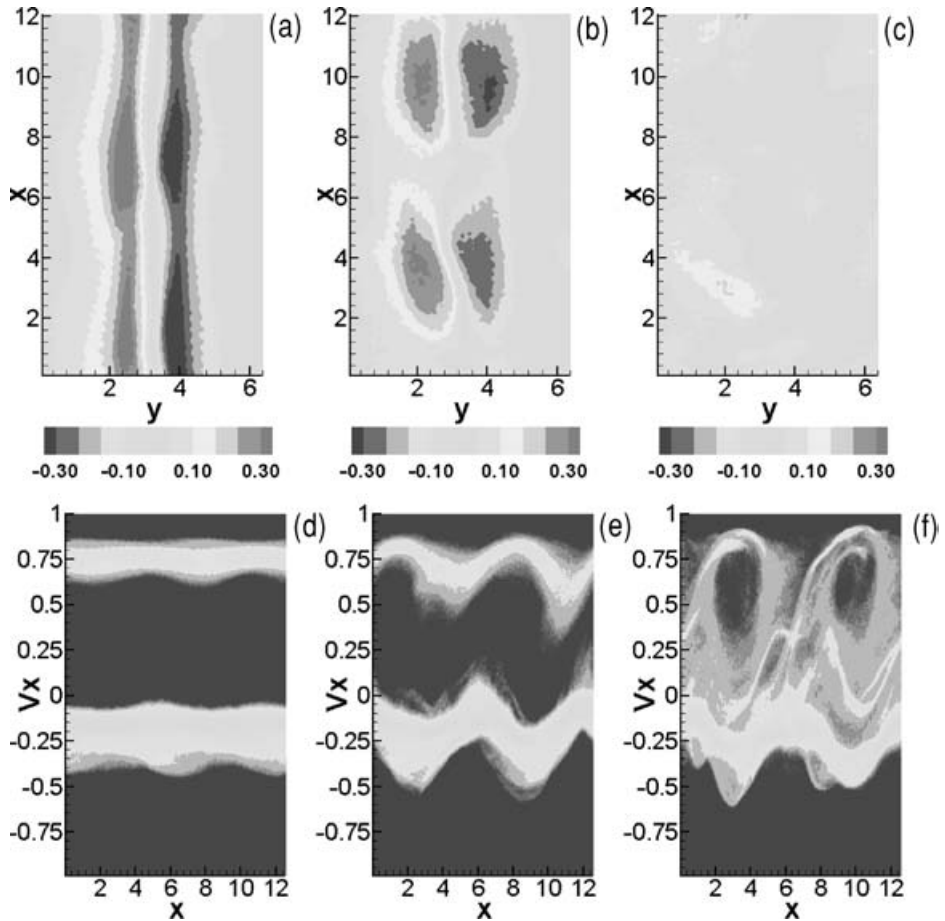
Figure 3. The first row is the contours of the magnetic field B_z and the second row is the electron distribution in (v_x, x) phase space average in the y direction at three times, (a), (d) $t = 20$, (b), (e) 30, (c), (f) 45.

times $t = 20$, 30 and 45. It can be clearly seen that particles in one streaming beam are about to pass another stream and wrap into vortices in phase space; that is, become trapped by E_x at $t = 45$. Some electrons even change their direction of motion in some regions along the x direction. This results in the longitudinal modulation of the magnetic field B_z, and the magnetic channel and the collimation of fast electrons disappear after $t = 45$. Figure 4 shows the simulation results with $v_{\mathrm{eth}} = 0.05c, v_{\parallel} = 0.15c$, i.e. the longitudinal distribution of the electron beams is wider than the case in Fig. 3, with all other parameters being kept the same. It can be seen from Figs 4(a)–(f) that the magnetic channel still remains until $t = 45$ owing to the suppression of ETSI. So it can be concluded that the narrow transverse distribution and the wider longitudinal distribution for beam electrons are beneficial for the stability of the magnetic channel.

Following, we focus on the aspect of relativistic electron generation in the interaction of a high-intensity laser beam at a dense plasma surface and propagation in the dense plasma. The influence of the self-generated magnetic and electric fields on
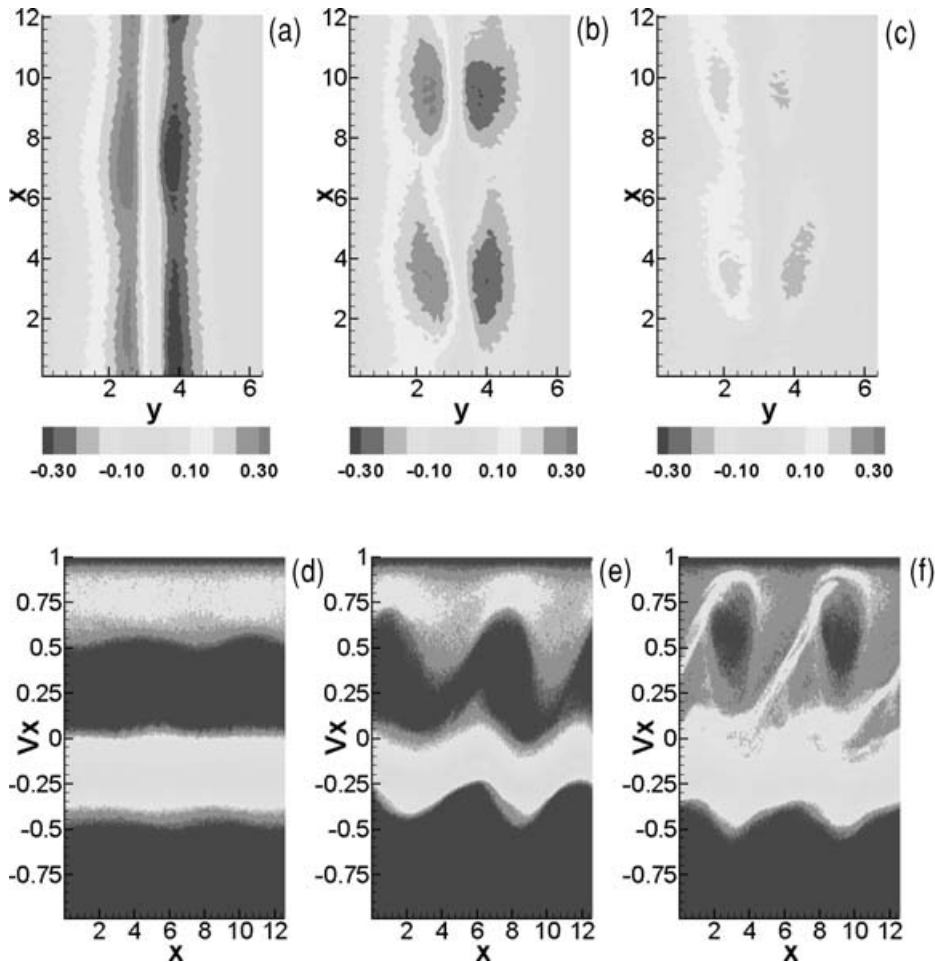
Figure 4. The first row is the contours of the magnetic field B_z and the second row is the electron distribution in (v_x, x) phase space average in the y direction at three times, (a), (d) $t = 20$, (b), (e) 30, (c), (f) 45.

the transport of relativistic electrons in a dense plasma was studied. The numerical results were obtained using the 3D PIC code LARED-P (see [13]). The simulation box is a cuboid. The number of spatial grid points is $200(y) \times 1000(x) \times 200(z)(4\lambda_0 \times 20\lambda_0 \times 4\lambda_0)$ with the total number of particles being 3.7×10^8; the initial plasma density is homogeneous in the transverse plane and has a length of $12\lambda_0$ with electron density n_e being ten times higher than the non-relativistic critical plasma density n_c, which corresponds to 1.1×10^{22} cm^{-3} for laser wavelength $\lambda_0 = 1$ μm. There is a $5\lambda_0$ vacuum region in front of the plasma and a vacuum region of $3\lambda_0$ at the back of the plasma. The initial plasma temperatures are $T_e = T_i = 1$ keV, $m_i = 1836m_e$. The laser beam is propagating from left to right along the x direction with an absorbing boundary for laser fields and a mirror reflection boundary for particles. Periodic boundary conditions are applied in the other two directions (y, z), i.e. the transverse plane. The laser polarization is in the z direction, and the pulse profile is transversely uniform and longitudinally semi-infinite, which rises up in
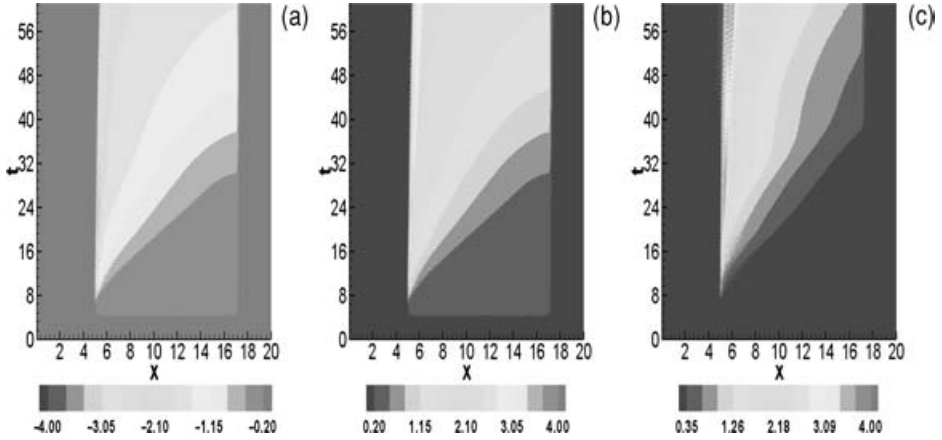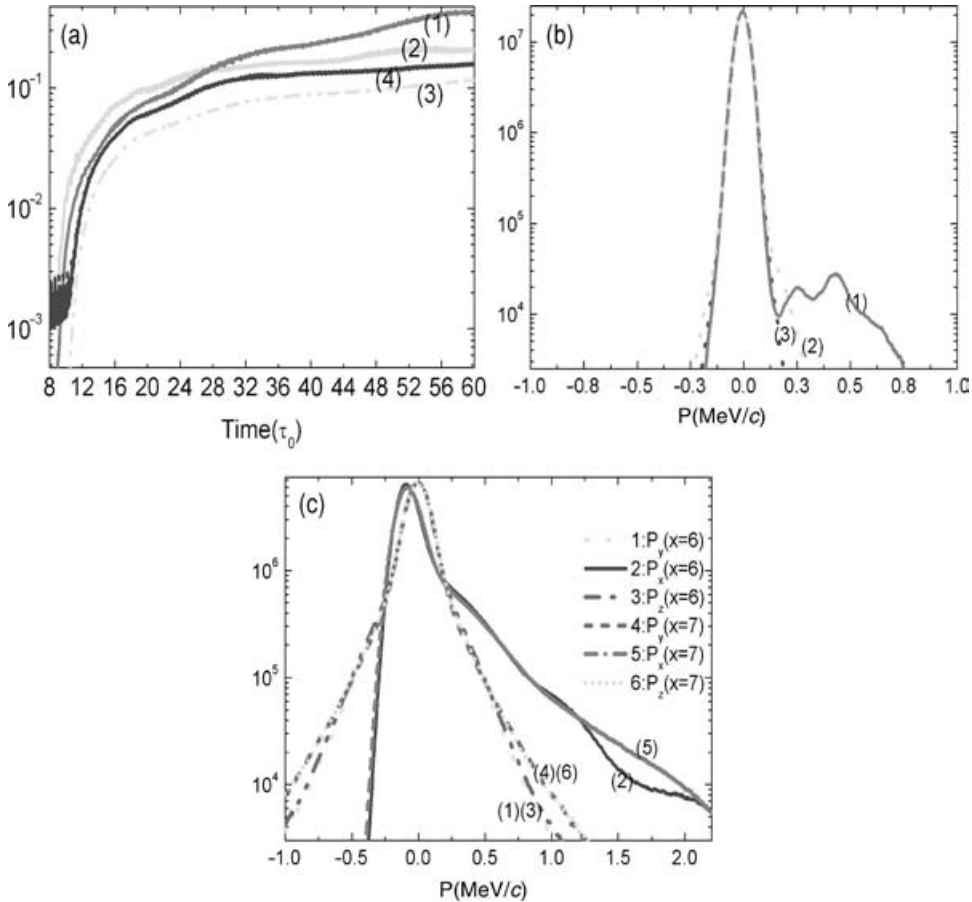
Figure 5. Time evolution of longitudinal electron current density integrated over the transverse plane (a) return current density; (b) forward current density; (c) time evolution of the forward power flux $(\gamma - 1)n_e v_x$ integrated over the transverse plane.

three laser cycles with a Gaussian profile. The maximum of the normalized vector potential is $a_0 = 2.7$, which corresponds to $I = 10^{19}$ W cm^{-2}.

The time evolution of the longitudinal electron current density $n_e v_x$ and the forward power flux $(\gamma - 1)n_e v_x$ (both integrated over the transverse plane) are presented in Fig. 5, which shows that the forward current is well neutralized as a whole in the transverse plane and the penetration speed of the forward electron current front is about $0.5c$ at $t = 10\tau_0, x = 6\lambda_0$, where τ_0 is the irradiated laser period. As time increases, the propagating speed of the front becomes slow, only $0.25c$ at $t = 14.5\tau_0, x = 6\lambda_0$. The forward power flux drops significantly over several λ_0 in the x direction as can be seen in Fig. 5(c). These pictures are similar to those shown in [3]. Figure 6(a) represents the time evolution of the longitudinal electric field energy and the transverse magnetic field (z component) energy integrated over the transverse plane at $x = 6.0\lambda_0$ and $x = 7.0\lambda_0$ (one or two laser wavelengths inside the dense plasma from the surface). One can clearly see that the WFI and ETSI have a sharp growth around $t = 8.5\tau_0$ at $x = 6.0\lambda_0$ and $t = 10.5\tau_0$ at $x = 7.0\lambda_0$, and the growth rate for WFI (ETSI) can be estimated from Fig. 6(a) as $\gamma_{\mathrm{ETSI}}(\gamma_{\mathrm{WFI}}) \cong 0.06(0.04)\omega_{\mathrm{pe0}}$. The saturation magnetic field B_z reaches about 20 MG. Figures 6(b) and (c) show the momentum distribution function of electrons averaged over one laser period at $t = 8.5\tau_0$, $x = 6.0\lambda_0$ and at $t = 14.5\tau_0$, $x = 6.0\lambda_0$; $t = 18.5\tau_0$, $x = 7.0\lambda_0$. From Figs 6(b) and 5(a) and (b) we estimate that $\langle v_y \rangle \cong 0.55c$, $n_b \approx 0.036n_{e0}$ around $t = 8.5\tau_0$ at $x = 6.0\lambda_0$ and a theoretical estimate for the linear growth rate of ETSI or WFI in the cold-fluid approximation is $\gamma_{\mathrm{ETSI}}(\gamma_{\mathrm{WFI}}) \cong 0.14(0.08)\omega_{\mathrm{pe0}}$. These values would be decreased if the spread of momentum of beam electrons were considered. From Fig. 6(a), we can also see that the longitudinal electric field energy exceeds the magnetic field energy at the position $x = 7.0\lambda_0$. This phenomenon is similar to the 2D PIC simulation results (Fig. 2). Figure 6(c) illustrates the electron momentum distribution, curves 1–3 are at ($t = 14.5\tau_0$, $x = 6.0\lambda_0$) and curves 4–6 are at ($t = 18.5\tau_0$, $x = 7.0\lambda_0$). These two points are on the same isoline of forward current density shown in Fig. 5(b). The distribution of forward electron momentum P_x is almost the same (about 0.47 MeV/c) at the two positions in the x direction ($x = 6.0\lambda_0$ or $x = 7.0\lambda_0$) but the transverse distributions of electron momentum

Figure 6. (a) Time evolution of the longitudinal electric field energy $|E_x|^2$ and the transverse magnetic field energy $|B_z|^2$ integrated over the transverse plane. Curve 1 is for $|B_z|^2$ and curve 2 is for $|E_x|^2$ at $x = 6.0\lambda_0$; curve 3 is for $|B_z|^2$ and curve 4 is for $|E_x|^2$ at $x = 7.0\lambda_0$. (b) Electron distribution with momentum at $t = 8.5\tau_0, x = 6.0\lambda_0$ averaged over one laser period. (c) Electron distribution with momentum. Curves 1–3 are at $t = 14.5\tau_0$ and $x = 6.0\lambda_0$; curves 4–6 are at $t = 18.5\tau_0$ and $x = 7.0\lambda_0$.

are significantly different. At $x = 6.0\lambda_0$, the transverse momentum spread $P_{y(z)}$ is about $0.15\,\mathrm{MeV}/c$, and the threshold for the occurrence of WFI is about $\alpha_{\mathrm{th}} \approx 0.10$, as predicted for the above parameters in (7). While at $x = 7.0\lambda_0$, the transverse momentum spread $P_{y(z)}$ is about $0.23\,\mathrm{MeV}/c$, $\alpha_{\mathrm{th}} \approx 0.24$. Using the data obtained from Fig. 5(b) ($n \cong 0.12n_{e0}, \alpha \approx 0.12$), the threshold for the occurrence of WFI is exceeded for beam conditions at $t = 14.5$, $x = 6.0\lambda_0$ but the growth rate is much smaller. For beam conditions at $t = 18.5$, $x = 7.0\lambda_0$, WFI can be quenched when the measured beam density is less than the threshold $\alpha_{\mathrm{th}} \approx 0.24$. The magnetic channel can provide an efficient means of directional fast electron transport and prevent the larger angular spread of the fast electrons. So by comparing the 3D results with the 2D PIC simulation results, we can draw the conclusion that the excitation of longitudinal field by ETSI may be the dominant factor in limiting the deep propagation of fast electrons.

4. Conclusion

In this paper, we studied the onset and nonlinear coupling of WFI and ETSI of electron beams propagating in dense plasmas by using PIC simulations. The beam electrons for fast ignition conditions are relativistic and have significant energy spread along or perpendicular to the propagation direction of the beams, which influences the growth rate, the instability threshold and the competition between WFI and ETSI. The narrow transverse distribution and the wider longitudinal distribution for beam electrons are beneficial for the stability of the magnetic channel. WFI can be completely suppressed if the transverse spread of the electron momentum is large enough, and the excitation of the longitudinal electric field influences the stability of the magnetic channel and may limit the deep propagation of relativistic electrons in dense plasmas. Using a 3D PIC code, we studied the generation of relativistic electrons in the interaction of a high-intensity laser beam at a dense plasma surface and the propagation of the electrons in the dense plasma. It was shown that the transverse collective heating suppresses WFI and the excitation of a longitudinal field due to ETSI may be the dominant factor in limiting the deep propagation of fast electrons.

References

[1] Tabak, M., Hammer, J., Glinsky, M. E., Kruer, W. L., Wilks, S. C., Woodworth, J., Cambell, E. M., Perry, M. D. and Mason, R. J. 1994 *Phys. Plasmas* **1**, 1626.

[2] Kodama, R. et al. 2001 *Nature* **412**, 798.

[3] Sentoku, Y., Mima, K., Kaw, P. and Nishikawa, K. 2003 *Phys. Rev. Lett.* **90**, 155 001. Sentoku, Y., Mima, K., Sheng, Z.-M., Kew, P. and Nishikawa, K. 2002 *Phys. Rev. E* **65**, 046408.

[4] Weibel, E. S. 1958 *Phys. Rev. Lett.* **2**, 83.

[5] Honda, M., Meyer-ter-Vehn, J. and Pukhov, A. 2000 *Phys. Rev. Lett.* **85**, 2128. Taguchi, T., Antonsen, T. M. Jr., Liu, C. S. and Mima, K. 2001 *Phys. Rev. Lett.* **86**, 5055.

[6] Malkin, V. M. and Fisch, N. J. 2002 *Phys. Rev. Lett.* **89**, 125 004.

[7] Wilks, S. C., Kruer, W. L., Tabak, M. and Langdon, A. B. 1992 *Phys. Rev. Lett.* **69**, 1383. Wilks, S. C. and Kruer, W. L. 1997 *IEEE J. Quantum Electron.* **33**, 1954. Pukhov, A., Sheng, Z.-M. and Meyer-ter-Vehn, J. 1999 *Phys. Plasmas* **6**, 2847.

[8] Califano, F., Pegoraro, F. and Bulanov, S. V. 1997 *Phys. Rev. E* **56**, 963.

[9] Boyd, T. J. and Sanderson, J. J. 2003 *The Physics of Plasmas*. Singapore: World Scientific, Ch. 7.

[10] Silva, L. O., Fonseca, R. A., Tonge, J. W., Dawson, J. M. and Mori, W. B. 2002 *Phys. Plasmas* **6**, 2458.

[11] Birdsall, C. K. and Langdon, A. B. 1985 *Plasma Physics via Computer Simulation*. New York: McGraw-Hill.

[12] Califano, F., Cecchi, T. and Chinderi, C. 2002 *Phys. Plasmas* **9**, 451.

[13] Zheng, C. Y., He, X. T. and Zhu, S. P. 2005 *Phys. Plasmas* **12**, 044505.